Supplementary Material for "Addressing Anthropogenic Noise and Electrical Anisotropy Hints in Magnetotelluric Data from the Annecy Area (French Pre-Alps)"

Contents of this file

Additional supplementary files uploaded separately

1. Observed and predicted transfer functions isotropic model (misfit_iso_all.pdf)
2. Observed and predicted transfer functions anisotropic model (misfit_ani_all.pdf)

1 Regional cross-section of the WAMB

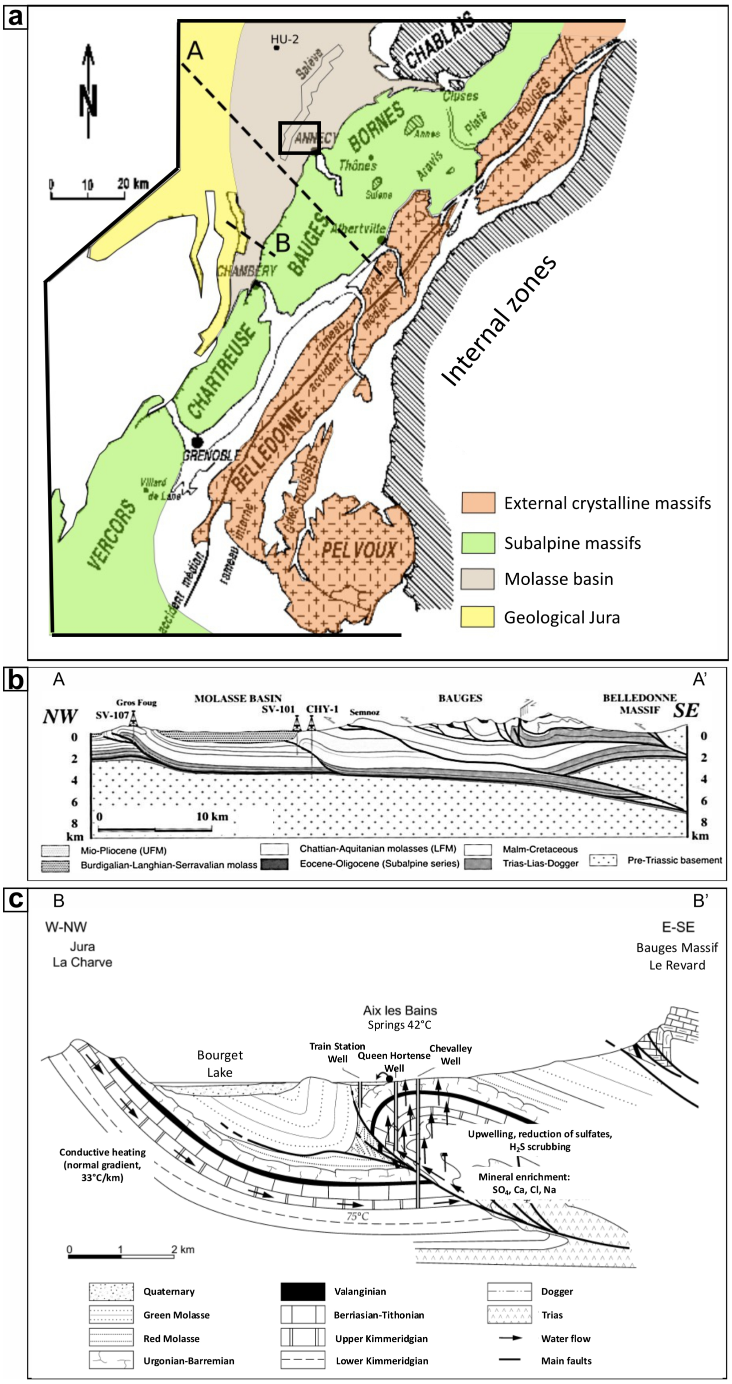

Figure S1. (a) Map of structural units from the WAMB (Beck et al 1998). The black solid rectangle represents the study area. (b) A-A' cross-section of the external part of the Alps, close to the study area (Beck et al 1998). (c) B-B' cross-section crossing the Aix-les-Bains area, showing the geological structures, thermal water circulation, and mineral and thermal water wells (Carfantan et al 2003).

2 Location of the reference stations

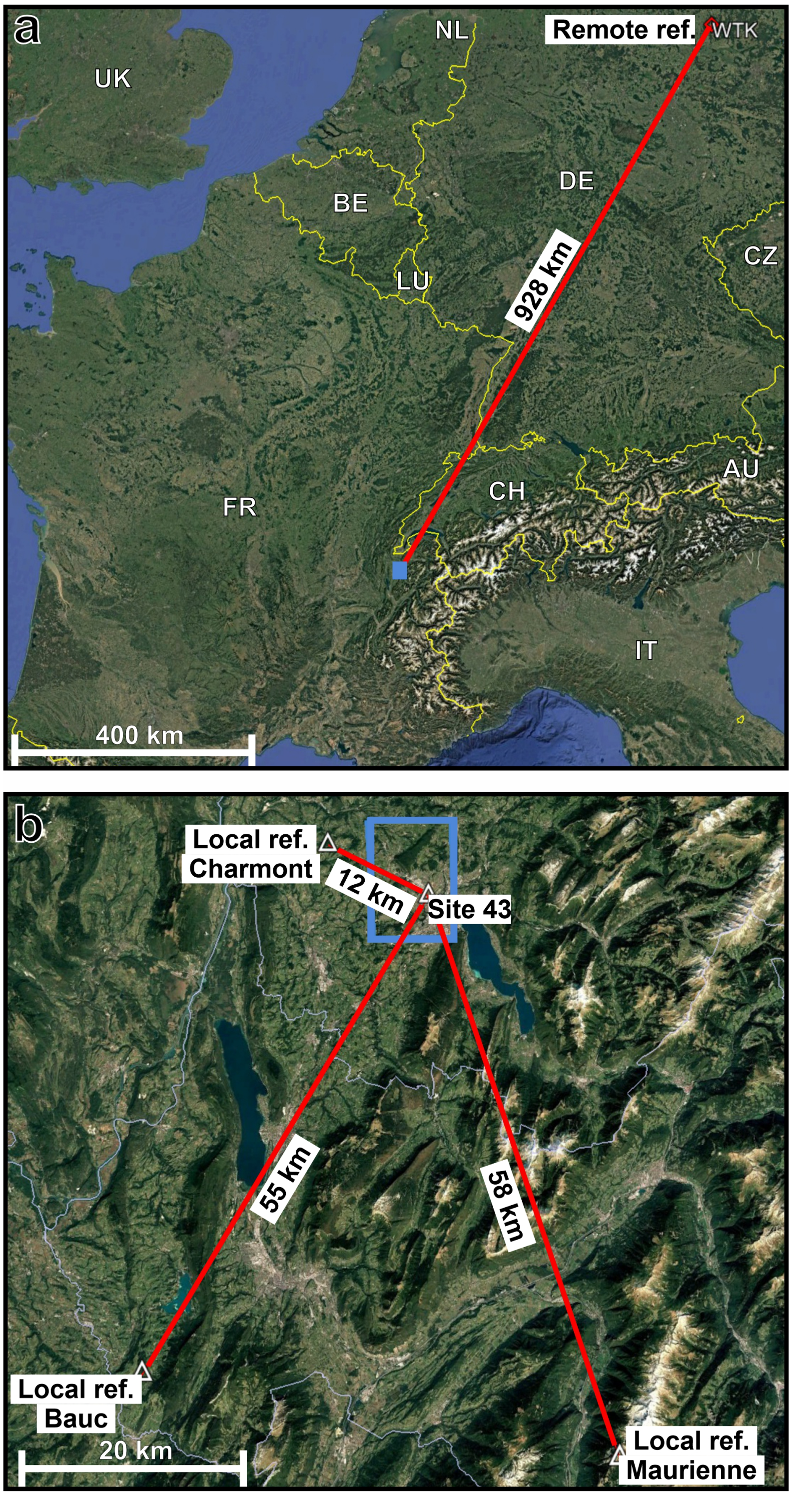

Figure S2. Location of the (a) remote and (b) local reference magnetotelluric stations used to process the survey.

3 1D inversion

After conducting the dimensionality analysis, we tested 1D inversion using the RJMCMCMT isotropic code by Brodie and Jiang (2018b). 1D inversion was performed using a probabilistic trans-dimensional Markov Chain Monte Carlo method implemented in the RJMCMCMT code Brodie and Jiang (2018a). The MCMC 1D inversion has the disadvantage of a strong assumption on the geological structure but its advantage is not to depend on regularization (prior model and smoothing); the parameter space can be fully explored and global minimum found. This code allows for two different kinds of input, either the real and imaginary parts of the Berdichevsky invariant of the impedance tensor (Berdichevsky et al 1980; Berdichevsky and Dmitriev 2008).

$$Z_{det} = \sqrt{(Z_{xx}Z_{yy} - Z_{xy}Z_{yx})} \tag{1}$$

or averaged apparent resistivity and phase data, namely the geometric mean of the apparent resistivity and the arithmetic mean of the phase Brodie and Jiang (2018a).

$$\hat{\rho} = \sqrt{\rho_{xy}\rho_{yx}} \qquad \hat{\theta}_{det} = (\theta_{xy} + \theta_{yx})/2 \tag{2}$$

The rotational invariant Z_{det} was chosen for inversion in a frequency range from 10^3 Hz to to 25 s. Data errors are considered as estimated by the FFMT processing. The burn samples were $2 \cdot 10^4$, from a total samples of 10^6. A maximum of 40 layers were considered, with an interface depth of 5000 m and 400 depth bins, the resistivity range from 0.1 to $10^6\,\Omega$m, with a quantity of resistivity bins of 400 and a credible interval of 0.9.

1D inversion models for each MT site are shown in figures S5 and S6 for comparison with the 3D isotropic inversion.

4 3D models

4.1 Choice of prior model and smoothing constrain values for 3D inversion

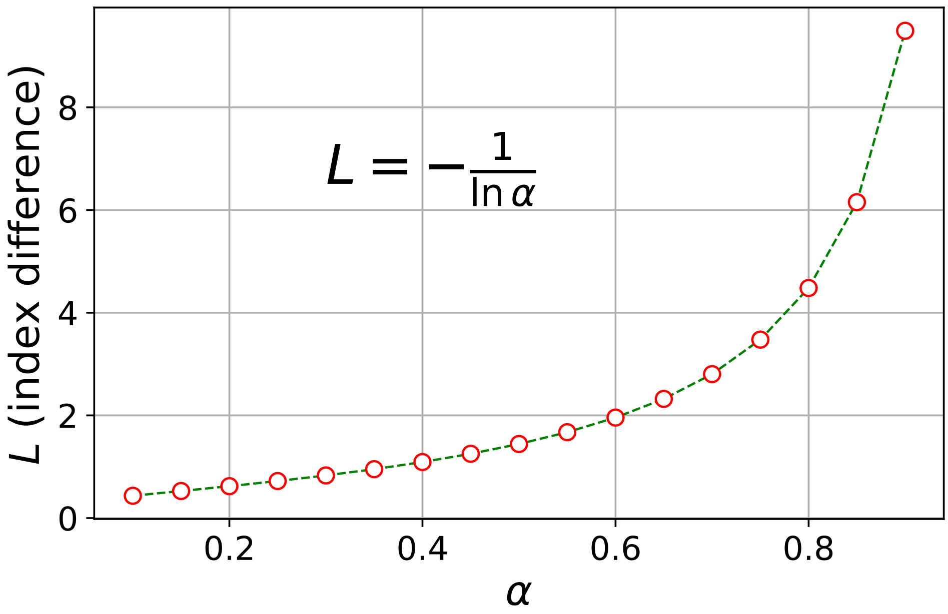

Figure S3. Nonlinear relationship between parameter α used in ModEM, and the correlation length L defining the exponential covariance assumed in this inversion code (Rodgers 2000).

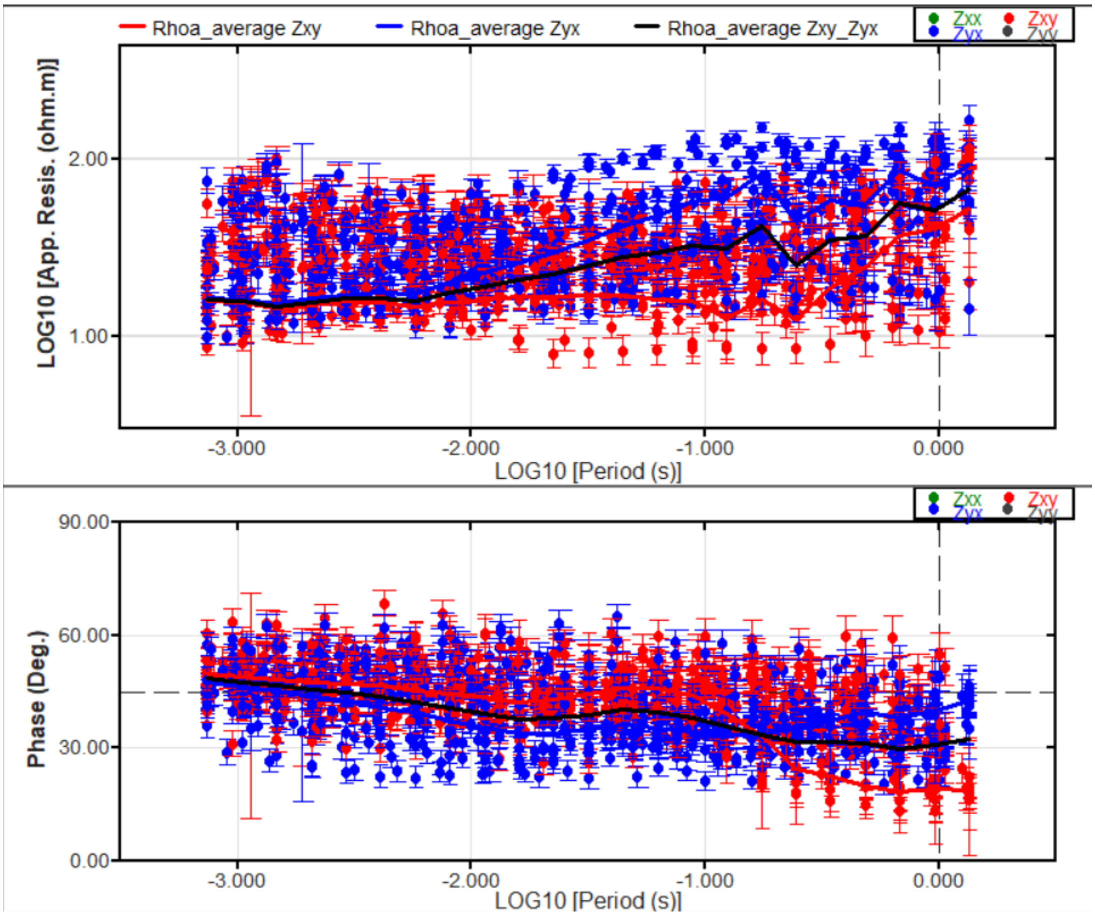

Figure S4. Apparent resistivity and phase curves from 46 magnetotelluric (MT) stations deployed around the Vuache Fault. The apparent resistivities (upper panel) and phases (lower panel) were calculated from the off-diagonal components of the impedance tensor **Z**. The red and blue solid lines represent the averaged apparent resistivity and phase for each off-diagonal component (Z_{xy} and Z_{yx}), while the black line corresponds to the average of both components. The results show that the variability of the apparent resistivity ranges between 10 and 100 Ωm.

Prior model resistivity values were tested for 12, 50 and 100 Ωm. For the inversion, a period range between 0.001 and 40 s was chosen according to the results from Figures S3 and S4.

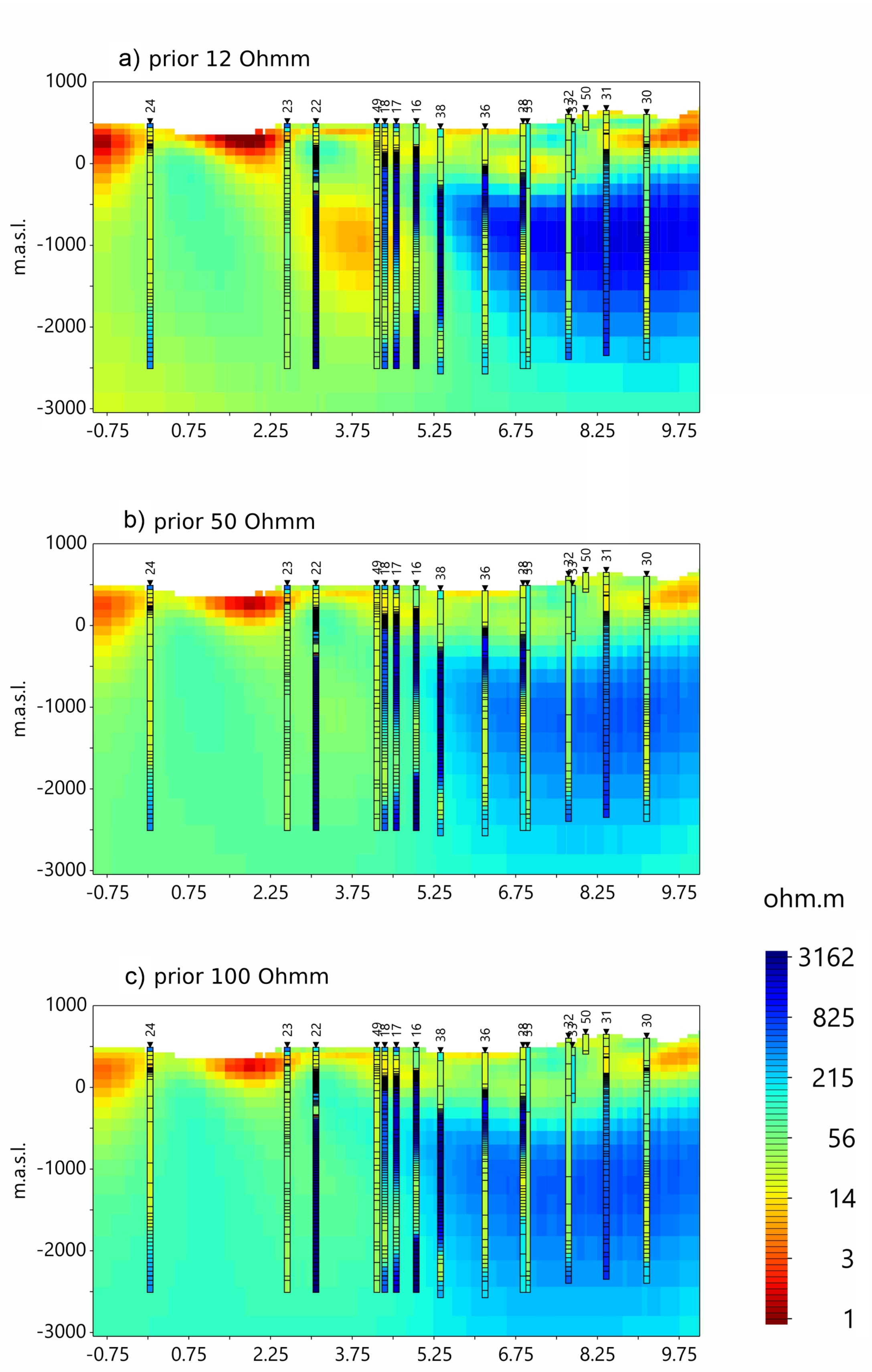

Figure S5. Influence of the prior model on the final model. Cross-section along the profile P2 (Figure 12 in main text for reference) for models M1.1–3 with homogeneous prior models (a) 12, (b) 50 and (c) 100 Ωm.

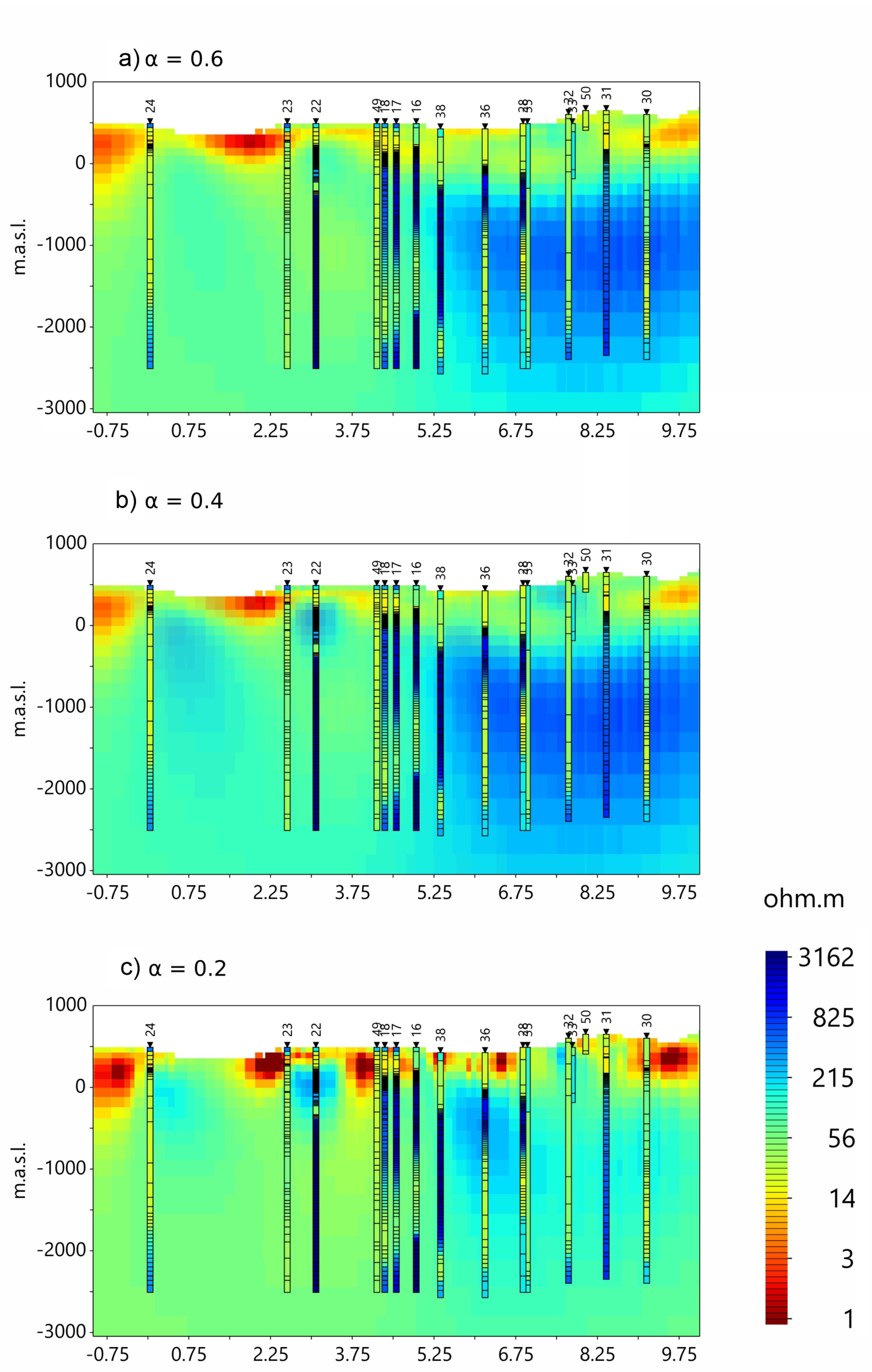

Figure S6. Influence of the smoothing parameter α on the final model. Cross-section along the profile P2 (Figure 12 in main text for reference) for models M1.4–6 with α = (a) 0.6, (b) 0.4 and (c) 0.2.

4.2 Model parameters

Table S1. Parameters for the isotropic M1.1 to M1.6 models

Parameter of the isotropic model without rotation		
Frequency range used		0.001 s to 40 s
		23 frequencies, 5 points per decade
	Horizontal	108×80 cells (160 m × 160 m), 15 padding cells.
	Vertical	60 cells, initial thickness: 60 m,
Mesh		growth factor: 1.13
	Topography	SRTM 30 m resolution, interpolated
	Rotation	0°
		$\sigma_{Zxx} = 0.1\sqrt{\lvert Z_{xx}Z_{xy}\rvert}$
Error floors Impedance		$\sigma_{Zyy} = 0.1\sqrt{\lvert Z_{yx}Z_{yy}\rvert}$
		$\sigma_{Zxy}, \sigma_{Zyx} = 0.05\sqrt{\lvert Z_{xy}Z_{yx}\rvert}$
Fixed errors Tippers		σ_{Tx}, $\sigma_{Ty} = 0.03$
Inversion parameter		ZT, Z
Prior models tested		10, **50**, 100 Ωm
nRMS		1.69, 1.68, 1.70
Correlation length α		0.6, **0.4**, 02
Total nRMS		1.7, 1.38, 1.23

Table S2. Parameters for the models tested in the study as in Table 2 of the main text, but with nRMS values given for the whole period range (0.001–25 s).

Model	Inversion	Rotation	Starting model	Damping λ	Damping λ_{ani}	Smoothing α	nRMS Z,T	nRMS Initial
M1.1-6	ZT, iso	0°	10-100 Ωm	10	-	0.2 - 0.6	1.23 - 1.72	3.8-4.5
M.ZT1	**ZT, iso**	**320°**	**50 Ωm**	**0.1**	-	**0.4**	**1.10, 1.16**	3.00
M.ZT2	ZT, P3	320°	M.ZT1	1	0.4	0.92, 1.08	0.97	3.00
M.ZT3	ZT, P3	320°	M.ZT1	10	0.4	0.92, 1.07	0.97	3.00
M.ZT4	ZT, P3	320°	M.ZT1	100	0.4	1.03, 1.21	1.14	3.00
M.ZT5	ZT, P3	320°	M.ZT1	1000	0.4	0.9, 1.05	0.95	3.00
M.ZT6	ZT, P3	320°	M.ZT1	10000	0.4	1.48, 1.58	1.51	3.00
M.Z1	Z, iso	320°	50 Ωm	1	-	0.6	1.46, -	3.71
M.Z2	**Z, P3**	320°	**M.Z1**	**1**	**10**	**0.4**	**0.83, -**	**3.71**
M.Z3	Z, P3	320°	M.Z1	1	1	0.4	0.94, -	3.71
M.Z4	Z, P3	320°	M.Z1	1	0.1	0.4	0.94, -	3.71
M.Z5	Z, P3	320°	M.Z1	1	100	0.4	0.84, -	3.71
M.Z6	Z, P3	320°	M.Z1	1	1000	0.4	1.07, -	3.71

4.3 Map view of the M.ZT1, M.ZT2 models

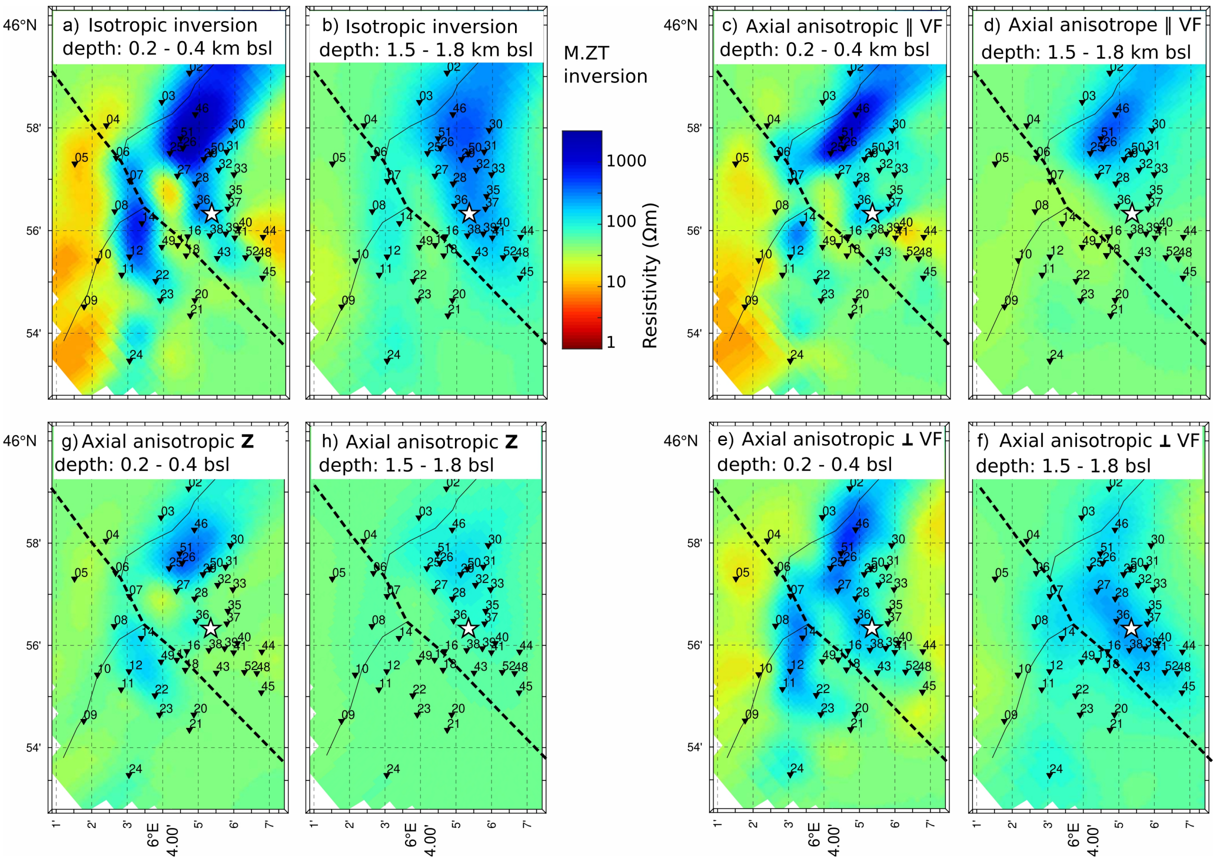

Figure S7. Map view as Figure 12 in the main text but for the M.ZT1, M.ZT2 inversion. (a, b) Isotropic ModEM inversion M.ZT1, and M.ZT2 principal resistivities; (c, d) parallel; (e, f) crossing the Vuache Fault; (g, h) in Z direction.

4.4 RMS map for M.ZT1, M.ZT2 models

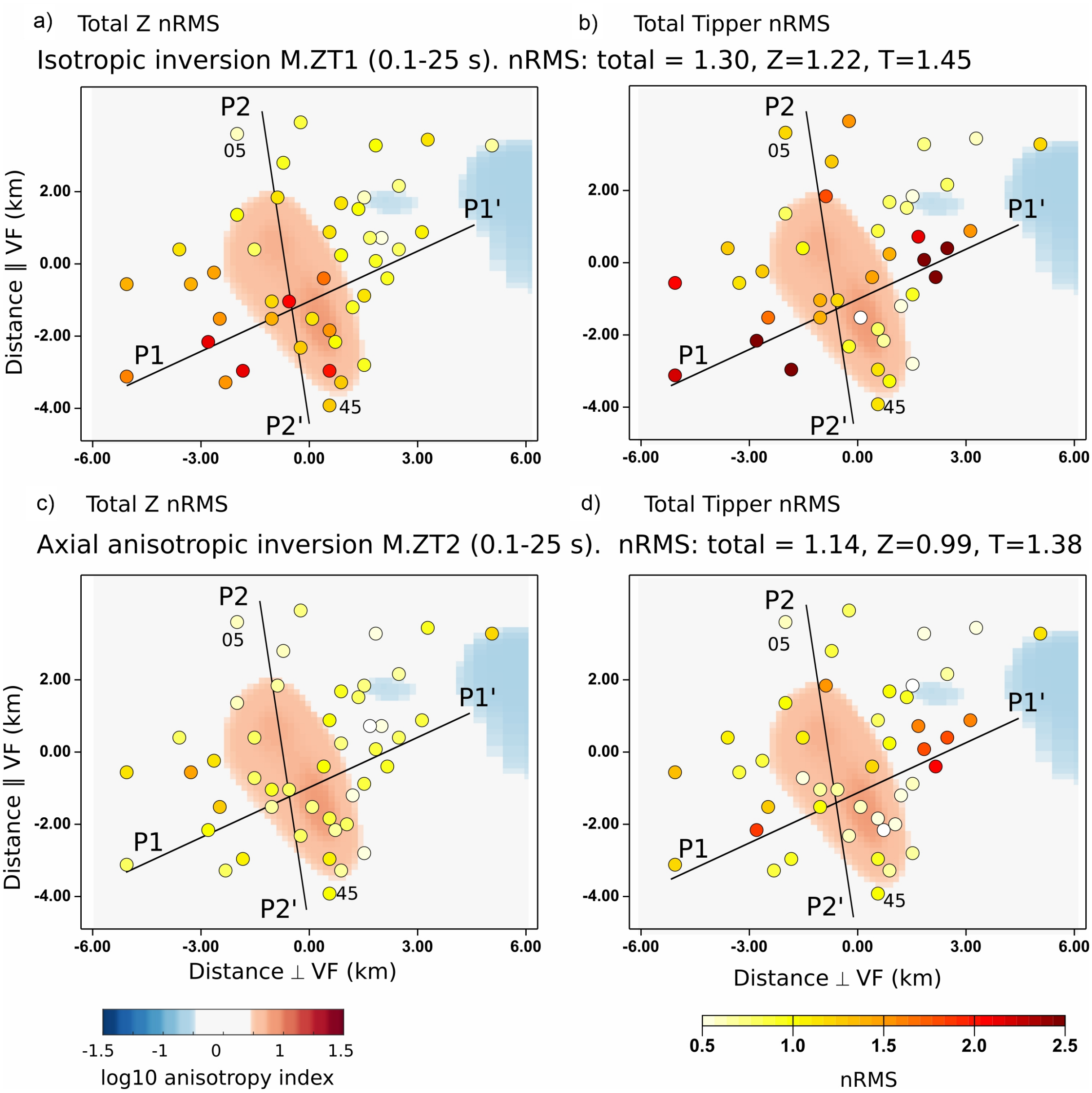

Figure S8. The misfit maps for joint inversions of impedance **Z** and tipper **T** in local coordinates: (a, b) isotropic model M.ZT1; (c, d) P3 model M.ZT2. Vertical axis corresponds to a direction parallel to the Vuache Fault (VF) and horizontal axis is normal to the fault. The nRMS is calculated for periods $> 0.1\,$s, for full impedance (a, c) and tippers (b, d). Color shows anisotropy index $\eta = \rho_{\perp\,\mathrm{VF}}/\rho_{\parallel\,\mathrm{VF}}$.

4.5 Seismicity and anisotropy index for M.ZT1, M.ZT2 models

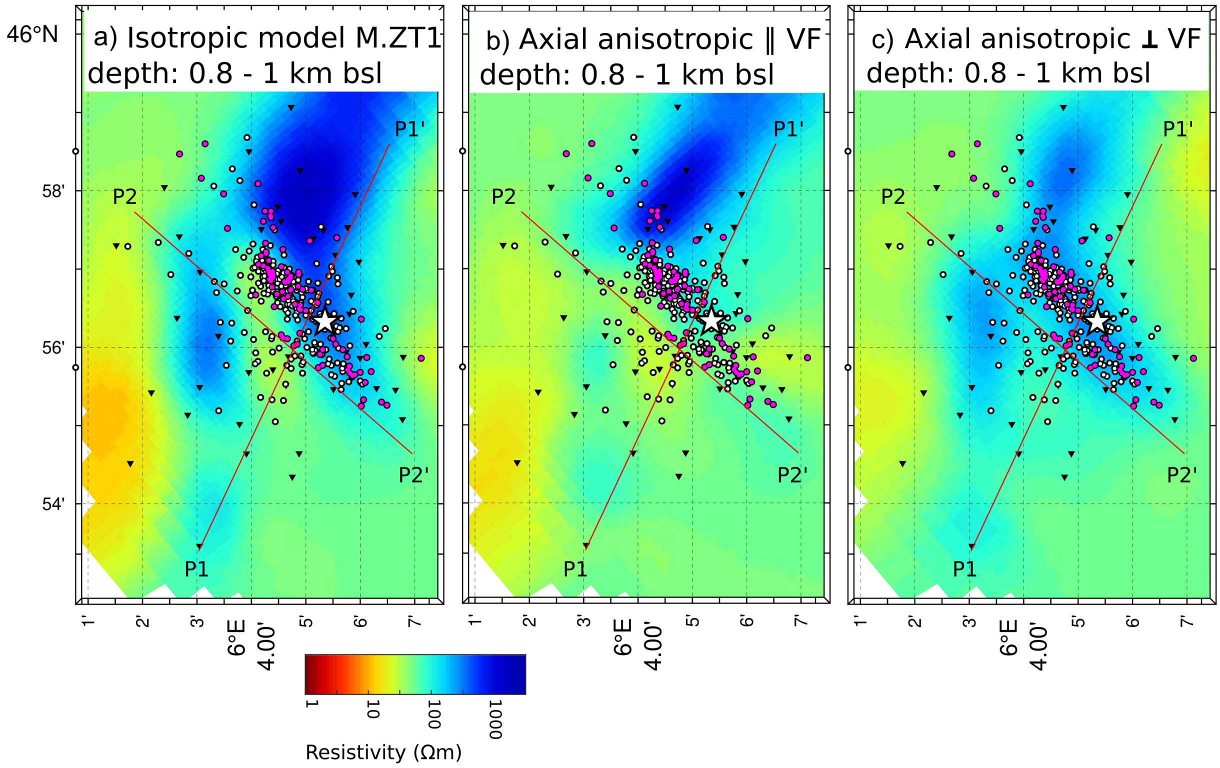

Figure S9. Map view of the M.ZT1, M.ZT2 models: (a) isotropic model M.ZT1; (b) $\rho_{\parallel \mathrm{VF}}$; (c) $\rho_{\perp \mathrm{VF}}$ principal resistivities of the anisotropic model M.ZT2. The Epagny 1996 earthquake (star) and its aftershocks (white circles) are shown after Thouvenot et al (1998). Magenta circles visualize the geometry of the Vuache Fault by a subset of aftershocks occurred "after day 10", and characterized by a diffusive behaviour (Got et al 2026). R1, R2, CR and C1 are the main features discussed in the text. Red lines show profile locations and black triangles MT sites.

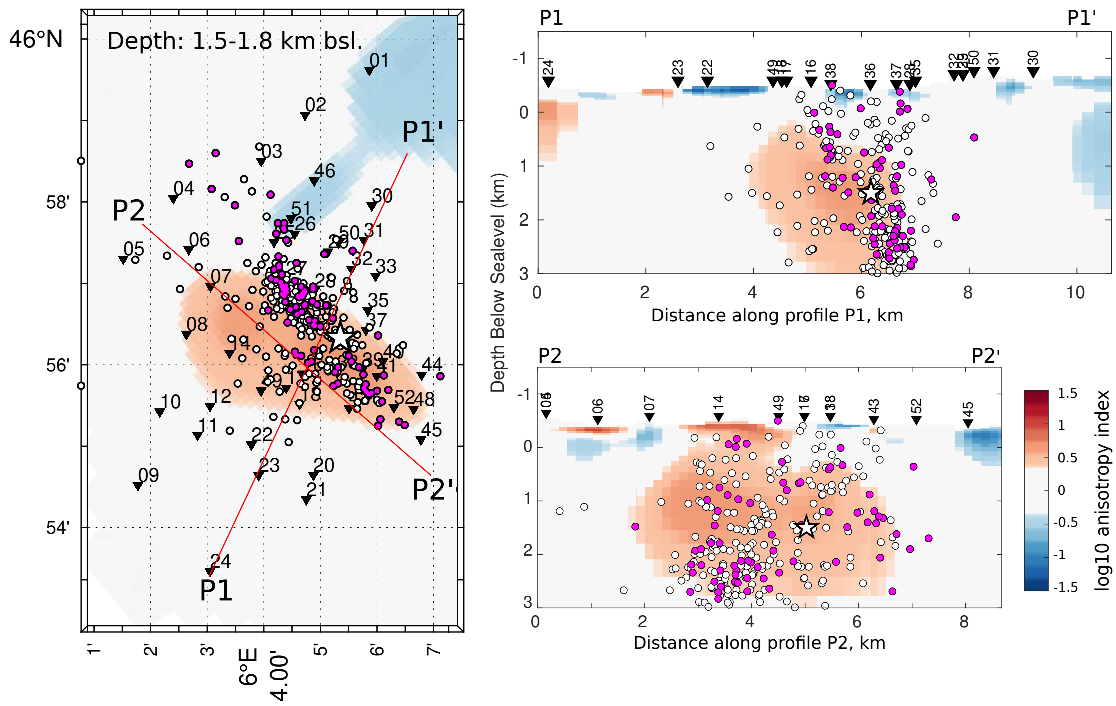

Figure S10. Horizontal anisotropy index ($\eta = \rho_{\perp \mathrm{VF}}/\rho_{\| \mathrm{VF}}$) for the model M.Z3 ($\lambda_{ani} = 0.1$) in map view and along profiles P1-P2. The red colors indicate higher conductivity parallel to the fault. Note the color scale difference to Figures 16 and 17 of the main text.

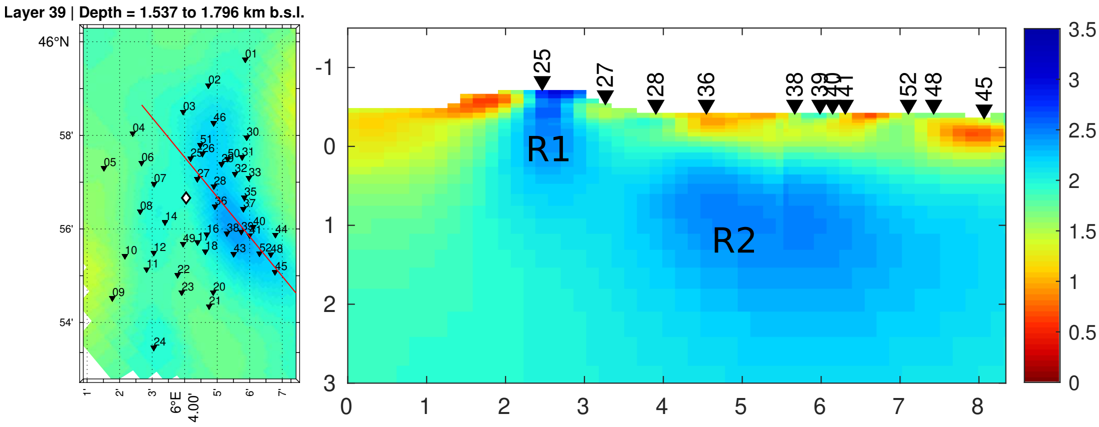

Figure S11. Connection between R1 and R2 bodies imaged with the anisotropic Z inversion normal to the Vuache fault MZ2.

References

Beck C, Deville E, Blanc E, et al (1998) Horizontal shortening control of middle miocene marine siliciclastic accumulation (upper marine molasse) in the southern termination of the savoy molasse basin (northwestern alps/southern jura). Geological Society Special Publications 134:263–278. https://doi.org/10.1144/gsl.sp.1998.134.01.12

Berdichevsky M, Dmitriev VI (2008) Models and methods of magnetotellurics. Springer, Berlin, https://doi.org/10.1007/978-3-540-77814-1

Berdichevsky MN, Vanyan LL, Kuznetsov VA, et al (1980) Geoelectrical model of the Baikal region. Phys Earth Planet Inter 22. https://doi.org/10.1016/0031-9201(80)90095-3

Brodie R, Jiang W (2018a) Trans-dimensional Monte Carlo inversion of short period magnetotelluric data for cover thickness estimation. ASEG Extended Abstracts 2018:1–7

Brodie RC, Jiang W (2018b) Trans-Dimensional Monte Carlo Inversion of Short Period Magnetotelluric Data for Cover Thickness Estimation. In: Proceedings of AEGC 2018, Sydney, Australia, https://doi.org/10.1071/ASEG2018abT5_1F

Carfantan JC, Nicoud G, Iundt F (2003) L'origine et le parcours des eaux thermo-minérales d'Aix-les-Bains (Savoie). In: 10ème journée technique du comité français de l'AIH: Circulations hydrothermales en terrain calcaire

Got JL, Wickham-Piotrovski A, Dufour A, et al (2026) Seismicity and hydro-mechanical coupling along strike-slip faults in flat-and-ramp structures : the case of the Vuache Fault in the Annecy Molasse Basin (French western Alps), https://doi.org/10.1093/gji/ggag240, manuscript accepted to Geophysical Journal International

Rodgers CD (2000) Inverse Methods for atmospheric sounding. World Scientific

Thouvenot F, Fréchet J, Tapponnier P, et al (1998) The ML 5.3 Epagny (French Alps) earthquake of 1996 July 15: a long-awaited event on the Vuache Fault. Geophysical Journal International 135(3):876–892. https://doi.org/10.1046/j.1365-246X.1998.00662.x